

Contour laser strategy and its benefits for lattice structure manufacturing by selective laser melting technology

Radek Vrána^{a,*}, Jan Jaroš^a, Daniel Koutný^a, Jakub Nosek^a, Tomáš Zikmund^b, Jozef Kaiser^b, David Paloušek^a

^a Brno University of Technology, Faculty of Mechanical Engineering, Institute of Machine and Industrial Design, Technická 2896/2, 616 69 Brno, Czech Republic

^b CEITEC - Central European Institute of Technology, Brno University of Technology, Purkyňova 123, 61200 Brno, Czech Republic

ARTICLE INFO

Keywords:

Laser powder bed fusion (L-PBF)
Selective laser melting (SLM)
AlSi10Mg aluminium alloy
Contour laser strategy
Transient thermal simulation
Finite element method (FEM)
SLM process simulation, porosity
Surface roughness
Dimensional accuracy
Lattice structure

ABSTRACT

This paper deals with the research of the Selective Laser Melting (SLM) scanning strategy to produce lattice structures from AlSi10Mg powder material. Nowadays, most of the SLM end-users use the laser strategy and parameters recommended by powder or machine suppliers to produce different components. However, this setup can cause material and shape imperfection, especially in the case of low-volume lattice structures. In this study, the default meander scanning strategy for AlSi10Mg material was changed to contour strategy and its main SLM process parameters were developed. Commonly used experiments were modified to consider the lattice structure's shape and dimension. The results showed that by using developed parameters, i.e., recommended range of input linear energy of 0.25–0.4 J/mm; track width based on strut diameter, input linear energy and the orientation of strut; the overlap of the laser contour tracks of 35% and inside-out direction; it is possible to produce lattice structures with high material density (more than 99.8%) and low surface roughness in a wide range of strut diameters from 0.6 to 3 mm. The differences in lattice structure production of vertical and inclined struts are described and discussed in relation to the SLM process during powder melting with use of thermal transient simulation.

1. Introduction

Additive technologies have become increasingly used to manufacture unique parts, mainly due to the ability to produce components with complex shape from a wide range of materials. It allows us to be inspired by the shape diversity of nature during the product design phase and to produce components with very few limits compared to conventional production. One of these unique shapes is a lattice structure with the potential for application in the aerospace or space industry due to a great weight to load ratio [1–4].

Selective laser melting (SLM) is a part of laser powder bed fusion (L-PBF) technology which is an additive technology that produces the components layer-by-layer using a high-energy laser to melt the fine metal powder. This technology allows processing of a wide range of metal materials from aluminium alloys to high-strength titanium alloys; therefore, it is a promising technology for various advanced industries. The SLM process is controlled by many process parameters that directly

influence the produced parts' quality and mechanical properties. The key parameters are those of the laser, i.e., laser power (LP), laser speed (LS), and the parameters of the scanning strategy, i.e., hatch distance (HD), overlap (OL), beam compensation (BC), and the type of used strategy (stripe, chessboard, contour etc.) [5–7]. The qualitative issues of the wrong setting of SLM process were examined mostly on the volumetric parts [8–10]. The results showed that the main imperfections arise not only on the surface of the parts (surface roughness, dimensional accuracy) but also inside of the material (porosity, unmelted areas, inappropriate material structure). In case of low-volume lattice structure, the same imperfections occur; however, they behave differently during SLM manufacturing process as was shown by Dong et al. [11]. They manufactured thin tensile samples with various diameters from 1 to 5 mm and examined the diameter's size effect on porosity and mechanical properties. The results showed that the porosity and mechanical properties were unstable for dimensions below 4 mm, i.e., the porosity increased, and mechanical properties decreased. It follows that

* Corresponding author.

E-mail addresses: Radek.Vrana@vut.cz (R. Vrána), Jan.Jaros2@vut.cz (J. Jaroš), Daniel.Koutny@vut.cz (D. Koutný), Jakub.Nosek2@vut.cz (J. Nosek), Tomas.Zikmund@vut.cz (T. Zikmund), Jozef.Kaiser@vut.cz (J. Kaiser), David.Palousek@vut.cz (D. Paloušek).

<https://doi.org/10.1016/j.jmapro.2021.12.006>

Received 10 October 2021; Received in revised form 28 November 2021; Accepted 7 December 2021

Available online 6 January 2022

1526-6125/© 2021 The Society of Manufacturing Engineers. Published by Elsevier Ltd. All rights reserved.

for thin lattice structures, the default SLM process parameters led to worse results, and the parameters and laser strategy must be improved.

The results of the previous study could be closely associated with the lattice structure geometry usually composed of many thin inclined struts. The heat flow and dissipation of the thermal energy after laser melting are lower compared to full volumetric parts. It was shown by Delroisse et al. [12], who divided the inclined strut into the upper and bottom areas (above and below strut axis) due to the different quantity of an internal porosity observed by μ CT. The upper area of the inclined strut contained a porosity of 0.1% compared to the bottom area with a porosity of 4%. The same situation was observed in the BCC cell node by Liu et al. [13].

This thermal behaviour also contributes to the increase of surface roughness, as was shown by other studies [14–16], which can result in a change in thin-struts shape, as was shown in studies [17–20]. Han et al. [14] described two possible explanations for high surface roughness in down-skin areas. First, the commonly known stair effect, which arises due to layer-by-layer production and orientation of strut. The second is the melt pool's flowability, which is in the liquid phase for a longer time due to the accumulation of thermal energy in the low-volume struts. Then, the melted material can flow deeper into the surrounding powder bed and the powder particles could be entrapped on the strut surface.

One way to reduce the consequences of the thermal accumulation is to reduce the input laser energy by modification of the SLM process parameters. However, it is also necessary to modify the SLM scanning strategy because they are strongly connected, as was described in many studies [10,15,21–27]. The authors [21,22] showed LP and LS's effect on the single-track width. As LP increased and LS decreased (i.e., the input laser energy increased), the single weld-track width increased. The authors [21,23] defined the key weld track parameters, i.e., depth and width of the track, which ensure the right connection between neighbouring tracks and previous layers as well as the height of the track, which must be close to the applied layer thickness. Tian et al. [15] measured the contact angle between single track's surface and base plate. A contact angle higher than 90° led to the formation of a balling effect, which could cause a higher porosity between neighbouring track welds due to unmelted powder particles. Other authors focused on the overlapping of the neighbouring tracks [10,25]. They found out that too low HD led to spherical porosity between weld tracks due to material overheating and following material evaporation. Due to the fast solidification of melted material, the vapours were trapped inside the material.

On the other hand, the large HD causes poor or no connection between the neighbouring single-tracks and trapping of the unmelted powder between them [28]. According to the melt pool behaviour, the composition of the powder is also related to the porosity between single tracks. Louvis et al. [26] described that the AlSi10Mg alloy formed an oxide film at the melt pool's edges. Oxide film limits the melt pool flowability and causes porosity due to nonmelted powder particles closed between the laser tracks.

The SLM process parameters setting's influence was also examined directly on the lattice structure geometry. Qiu et al. [27] dealt with the lattice structures with a diameter of 0.3 mm. Using a constant LS of 7000 mm/s and increasing LP (in the range of 150–400 W) the diameter of struts was increased in the range of 0.26–0.5 mm. By using a constant LP of 400 W and increasing LS (in the range of 1000–7000 mm/s), the struts' diameter was decreased in the range of 0.8 to 0.6 mm. It follows that the parameters setup directly influences the final dimensions of the lattice structure and thereby the mechanical properties. Vrána et al. [16] performed a complex study that described the influence of the main SLM process parameters (LS, LP, HD) directly on the lattice structure imperfections such as internal porosity and surface roughness. They also used special contour strategy to reach relative density of AlSi10Mg low-volume material of 99.83%. The results showed a clear dependence of porosity and surface roughness on the input energy. However, the study was performed only for the strut diameter of 2 mm, and the results for

other sizes could differ, as was shown by Dong et al. [11]. The scanning strategy for lattice structure production was also dealt with Pauly et al. [7]. They used three different scanning strategies to produce a thin strut geometry - chessboard strategy (small pores; $\rho_{rel} = 97.2\%$), stripe strategy (sharp pores; $\rho_{rel} = 98.5\%$), contour strategy (small round pores; $\rho_{rel} = 97.7\%$). The results showed that the strategy could significantly influence mechanical properties due to the shape of the pores and the porosity level.

Mechanical properties of low-volume lattice structures had higher susceptibility to material imperfections when the universal SLM process parameters were used [29,30]. These authors used recommended process parameters for lattice structures production and significant surface roughness and dimensional deviation (between -7.5% to -12.5%) were obtained. These deviations resulted in large differences in simulated mechanical properties using nominal dimensions of lattice structures and finally, the actually measured geometry had to be used to predict correct mechanical behaviour. The final results showed a strong correlation between computed and experimental mechanical properties. Kempen et al. [9] showed the influence of borderline porosity on mechanical properties. The porosity was generated by used scanning strategy and affected mechanical properties.

Based on the previous results, this study will focus on improving the lattice structure production using the contour laser strategy approach. The main goal is to find out a dependence of the main SLM process parameters on the lattice structure dimensions (dimensions up to 3 mm) and to reach stable and predictable lattice structure parameters such as porosity, surface roughness, and dimensions after SLM production.

2. Materials and methods

For better orientation in present study, a brief experiments workflow was created. The detailed description of the used materials and methods is further in the chapter.

To define the contour laser strategy (CS) parameters, the following workflow must be performed:

- Single weld tracks experiment - the perspective SLM process window was defined based on the visual and digital-light microscope results (Table 2).
- Thin wall/ hollow strut experiment - the single weld track sample was changed to 3D shapes of wall and hollow strut samples that includes the thermal conditions during lattice structure manufacturing. The larger dimensions were obtained compared to the single weld track experiment (Fig. 11).
- The key 3D dependence - diameter (d) vs. input linear energy (LE) vs. hollow strut thickness (HT) dependence was created that describe the change of the HT parameters and allows contour strategy parameters adjustment according to actual lattice structure geometry (diameter, orientation, Fig. 14).
- Overlap (OL) experiment - connection between two hollow strut walls was analysed. The optimum OL values were evaluated based on the porosity in the overlap area (Fig. 13).
- Porosity experiment (1st testing loop) - Based on the previous results, the contour strategy was designed. The porosity results showed imperfection (Table 5); therefore, the parameters were modified.
- Porosity experiment (2nd testing loop) - Significant improvement of porosity result was observed (Fig. 16); therefore, the dimensional and surface roughness analysis were performed.
- Porosity experiment (3rd testing loop) - The final fine tuning of a contour laser strategy was performed using d vs. LE vs. HT dependence. Various SLM parameter were defined as optimal for different strut diameter (Table 6).

2.1. Selective laser melting manufacturing

SLM machine (SLM 280^{HL}, Lübeck, Germany) equipped with a 400 W Ytterbium fibre laser has been used to manufacture all samples. The laser source had a Gaussian distribution and was focused on a spot diameter of 82 μm . The process conditions were constant for all produced batches of samples, i.e., the oxygen level was kept under 0.2% during the SLM process, the protective atmosphere of nitrogen was used, the platform was heated to 150 °C, the layer thickness of 50 μm was applied and the main SLM parameters were used based on the results of this study. All samples were produced from the gas atomised aluminium alloy AlSi10Mg (TLS Technik GmbH, Bitterfeld, Germany) with particle size distribution in the range of 15–60 μm (Fig. 1b).

2.2. The main contour laser strategy parameters

The basic SLM experiments described in the studies [13–15,21,23,24] were modified to consider the specific conditions during SLM manufacturing of low-volume lattice structures. The obtained parameters were used to define the parameters of the presented contour laser strategy shown in Fig. 1a, which are - laser power (LP), laser speed (LS), overlap (OL) and beam compensation (BC). Overlap (OL) defines sufficient connection between two laser tracks inside the strut and is determined by contour distance (CD). The exact value of OL can be found only for the known track width (HT). Beam compensation (BC) indicates the strut border's offset to achieve the required strut size.

2.2.1. Laser process parameters window

The single-track experiment aimed to describe the influence of the LP, LS laser parameters on the quality of the AlSi10Mg single track welds and thereby find a suitable process window include the consistent track welds with the known welds' width. Single track welds were produced on the top side of a 5 mm solid material block (Fig. 2b) and captured by a light microscope (Olympus SZX7, Olympus). The images were further used for track welds width measurement and visual evaluation of the single-track welds' continuity and uniformity. The track width (TW) was measured in twelve points along two single track welds (24 values) and the average value was evaluated (Table 2). During the experiment, the following parameters were changed - LP in the range of 175–400 W and LS in the range of 200–2000 mm/s.

2.2.2. Geometry of single-track welds

Based on the previous experiment, the second batch of single-track welds was focused on the track weld's geometry. The laser parameters were the same as in the previous test, but the ranges were narrowed according to the perspective process window, i.e., LP in the range of 200–350 W, LS in range of 500–1400 mm/s which corresponds to the input linear energy (LE) of 0.25–0.4 J/mm (expressed by Eq. (1)). The track weld geometry was measured on metallographic cross-sections using a digital-light microscope (Keyence VHX-6000, Z250R lens, zoom 250 \times).

The evaluated parameters were track weld width (1), height (2), and depth (3), as is shown in Fig. 2a.

$$LE = \frac{LP}{LS} \quad (\text{J/mm}) \quad (1)$$

2.2.3. Influence of the samples geometry

As was already mentioned in the introduction, the porosity and surface roughness are affected by a base material's thermal conductivity. The total thermal conductivity of the whole component then further depends on its shape and orientation. Therefore, the basic single-track experiment was modified in two steps to investigate their influence on the samples' shape. First, the geometry was changed into thin-wall geometry (3D single track) and then into the shape of the hollow strut, representing the geometry of lattice structure. Both modified geometries consist of one single track in each layer (Fig. 3b) that allows observing the changes caused by modified samples heat dissipation. The resulting thickness of the walls and hollow struts were compared with the single-track welds' width. The thin walls had a rectangular geometry of 10 \times 2 mm and were produced in two orientations, i.e., vertical and inclined (35.26°), that corresponds with BCC and BCC-Z lattice unit cells' basic geometry. The hollow struts samples were produced in the same two orientations with the diameters range of 0.3 to 3 mm. Various dimensions and two orientations of the samples were used to describe the influence of size and orientation effects on the hollow strut thickness. The laser parameters were used within the perspective process window of LP and LS (LP 200–350 W; LS 500–1400 mm/s). The geometry was measured on metallographic cross-sections using a digital-light microscope (Keyence VHX-6000, Z250R lens, zoom 250 \times). The thickness values were measured as the average values between the two lines, each was made by interpolation of five border points (Fig. 3a).

2.2.4. Overlap parameter

The overlap experiment was performed to ensure sufficient connection between neighbouring single-track welds and avoid excessive remelting of material in their connection that can initiate the inter-weld porosity. The sample's shape was a hollow strut composed of two laser tracks (Fig. 4b). The OL parameter was chosen in the range of 0–55% of the hollow strut thicknesses. The nominal diameters of the two tracks hollow strut were 0.8; 1.2; 1.6; 2 mm. The track OL was evaluated based on the internal porosity (image analyses, ImageJ, threshold 100) measured in connection to the two tracks (Fig. 4a). The results were evaluated from metallographic cross-sections captured by a digital-light microscope (Keyence VHX-6000, Z250R lens, zoom 250 \times).

2.3. Analysis of porosity, surface roughness and dimensional accuracy

The shape and dimensions of the component can significantly affect the formation of the SLM manufacturing imperfection [11]. Therefore, to obtain meaningful results, the sample's shape must be as close as

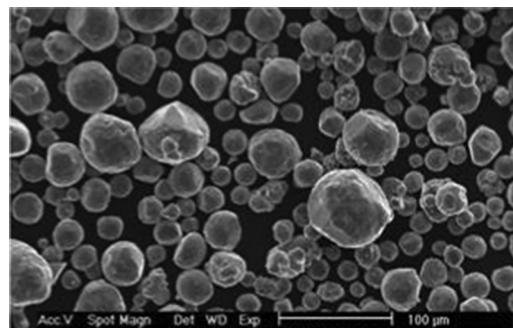
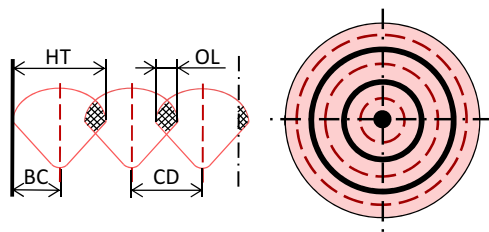


Fig. 1. (a) The parameters of the contour strategy: hollow strut thickness (HT), overlap (OL), contour distance (CD) and beam compensation (BC); (b) the shape of powder particles (scanned by SEM).

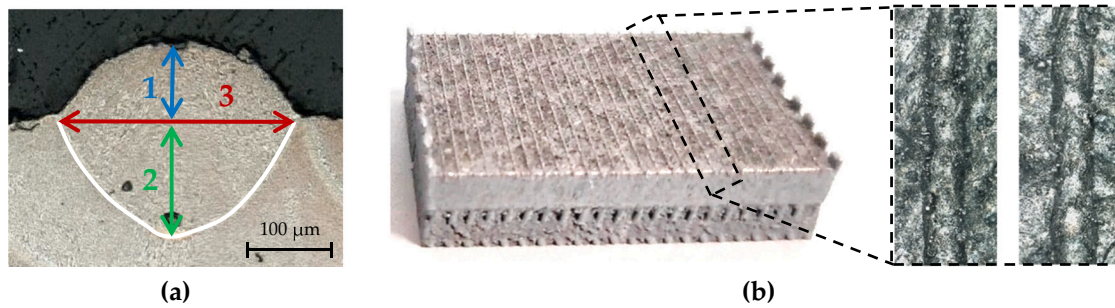


Fig. 2. (a) Measured geometrical parameters of the single-track welds; (b) the single-track sample.

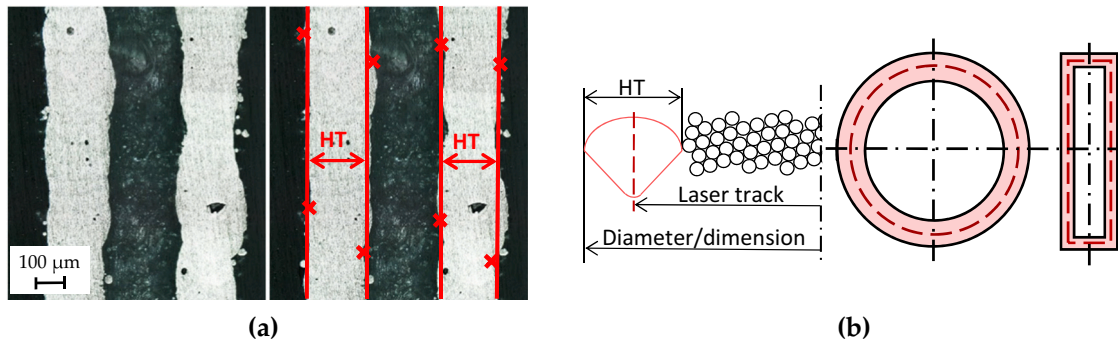


Fig. 3. (a) Methodology of the thin-wall and hollow strut thickness evaluation; (b) geometry of hollow strut and thin-wall.

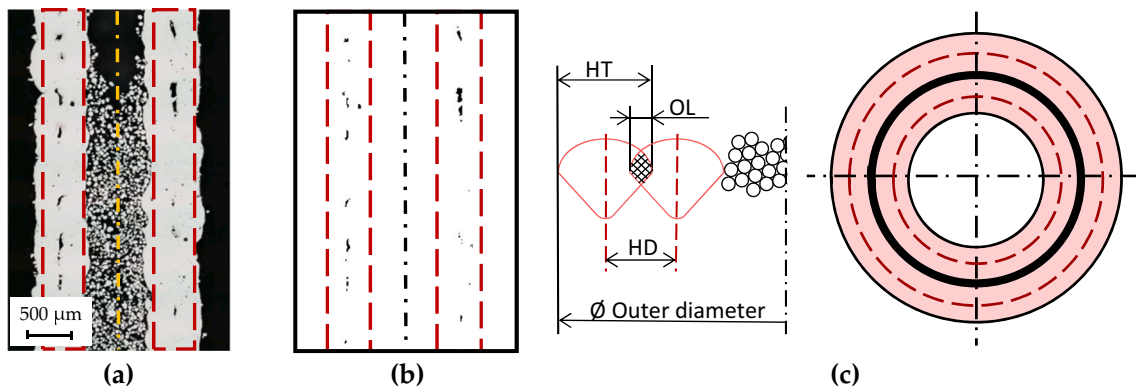


Fig. 4. Porosity measured in the connection of neighbouring laser tracks (a) metallographic cross-section of two track hollow strut, (b) the final monochrome image analysed by ImageJ software, (c) geometry of hollow strut consists of two laser tracks.

Table 1
The list of the applied SLM parameters in the study.

Parameters	1 st loop	2 nd loop	3 rd loop
Laser process param.	Values from previous hollow strut experiment		LP and LS according to RSA
Dir. of contour production	Outside-in	Inside-out	
Track width	Previous hollow struts results	Response Surface Analysis (RSA)	
Beam Compensation	1/2 of the thickness of the hollow strut samples	1/3 of the thickness of the hollow strut samples	
Overlap	30 %	35 %	

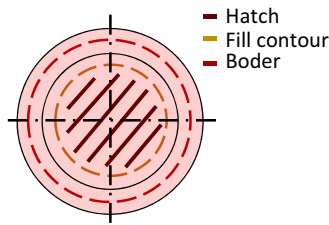


Fig. 5. The default SLM process parameters (a) schema of the meander strategy (b) table of the process parameters.

possible to the final part. In the case of the lattice structure, the strut geometry was chosen. The experiments were further focused on obtaining the porosity distribution, pores size, surface roughness and dimensional accuracy of the strut samples.

The struts were produced in two orientations, i.e., vertical and inclined (35.26°), that corresponds with BCC and BCC-Z lattice unit cells' basic geometry. The struts' diameters were used in the range of 0.6–3.0 mm, and the thickness of the track (HT) was set differently for each diameter according to the previous results. Other parameters were constant and were applied according to the testing loop, as is shown in Table 1.

Based on the first testing loop results, the influence of the contour track production order was evaluated on the level of porosity; therefore, the inside-out direction of production was applied in the second and third loops to reduce material imperfection for strut diameters over 1.0 mm. Moreover, finally, the OL was changed to 35% according to porosity results (Figs. 15b, 13) and the BC of 1/3 hollow strut thickness was used after the first results of dimensional analysis. All results were compared to the default SLM process parameters i.e., meander hatch strategy (Fig. 5a).

X	Hatch	Fill cont.	Border
LP (W)	350	250	300
LS (mm/s)	1150	555	600
LE (J/mm)	0.3	0.45	0.5
OL (%)	50	50	50
Laser focus	0	-4	0

2.4. Porosity analysis

The porosity was analysed in two ways. First, the porosity was evaluated in the connection of the two laser tracks by digital-light microscope. In this case, the cross-section images of the two tracks hollow strut were captured by the digital-light microscope (Keyence VHX-6000,

Z250R lens, zoom 250×) and analysed using ImageJ software. Then the porosity value was evaluated as the percentage of black in the monochrome images. The second, a micro-computed tomography approach (μCT, GE phoenix v | tome | x L240, Waygate technologies, Hürth, Germany) was used for porosity analysis in the whole volume of the strut samples and evaluation of the influence of contour strategy parameters on the occurrence of material imperfections (Fig. 6a). The following adjustment of the measurement was used i.e., a micro-focus X-ray tube with a voltage of 130 kV, a current of 100 μA and a 0.5 mm wide copper filter. The achieved linear voxel resolution was 16 μm for all samples with a minimal pore volume of 2 voxels. The scanned data were further reconstructed in the Datos reconstruction software and processed in VGStudio MAX 3.1 software (Fig. 6b,c,d,e). The threshold value was obtained automatically from common scan of all samples (Fig. 6a) and applied to segmented samples This was performed to ensure the comparability of the results of struts porosity [31]. The main outputs from the μCT analysis were 3D images of the material porosity for all produced struts (more than 232 samples), i.e., its level and distribution for each strut. The μCT was also used to digitize a struts shape to STL format which was used for dimensional accuracy and surface roughness analysis. These outputs enabled to find the dependences of porosity and surface roughness on the strut diameter and LE.

2.5. Shape and surface roughness analysis

$$R_a = \frac{1}{N} \sum_{i=1}^N |y_i| \text{ (}\mu\text{m)} \tag{2}$$

The surface roughness and shape of struts were investigated using the digitised STL data from μCT even though relatively high voxel size resolution of 16μm. The main purpose of this analysis was to use large data set from μCT analysis and find out dependences of these parameters according to the strut diameter and LE, not exact values.

The evaluation was performed in the GOM Inspect software by the following procedure. First, the digitalised data was aligned to CAD data using the Best fit method. The surface roughness was measured as dimensional deviation from CAD in 200 points of line selection on the down-skin surface of the inclined strut (Fig. 7a). The deviations were converted to Ra surface roughness according to Eq. (2). Then, the strut's actual diameter was measured by fitting an ideal Gauss cylinder (used selected point: 3 sigma) to the largest possible area of the digitalised data (Fig. 7b).

2.6. Numerical simulation

The transient thermal simulation was performed in Ansys Workbench software to clarify the observed effects in porosity and surface

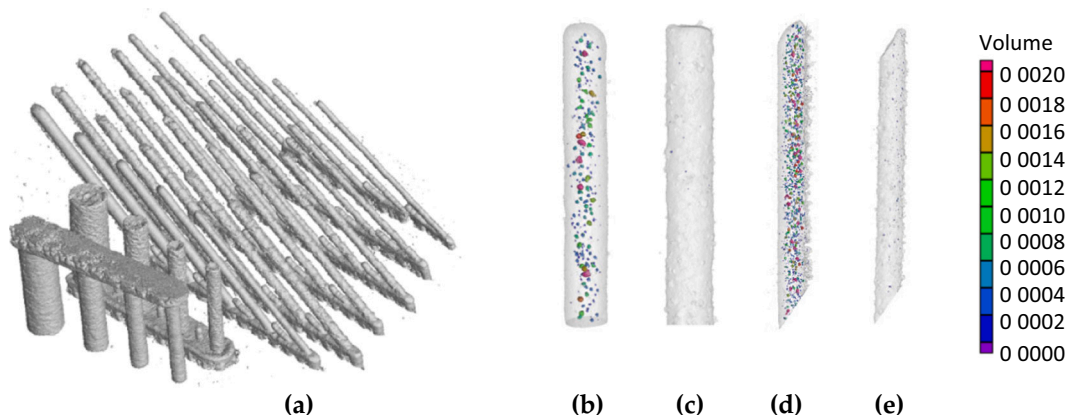


Fig. 6. Porosity analysis (a) group of samples scanned together, (b), (c) internal porosity of vertical struts, (d), (e) inclined struts.

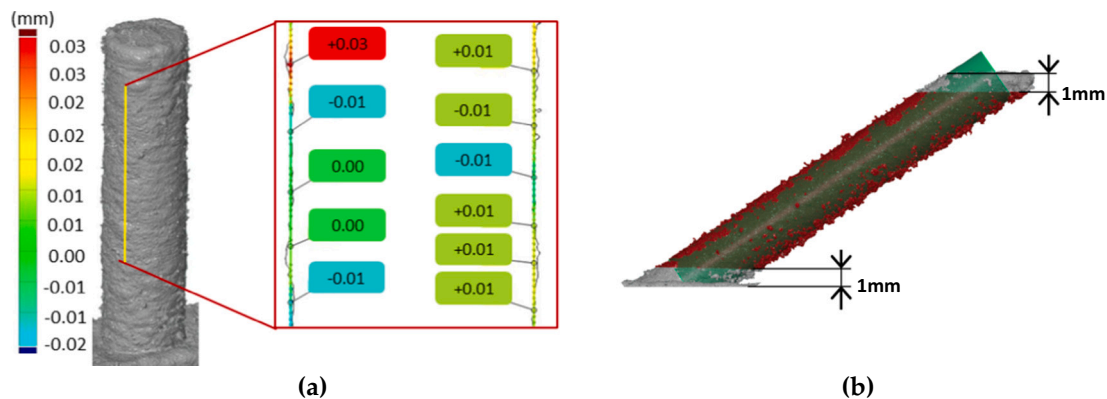


Fig. 7. (a) Surface roughness analysis on a vertical strut, (b) the inclined strut with fitted Gauss cylinder and red marked area of selection. (For interpretation of the references to colour in this figure legend, the reader is referred to the web version of this article.)

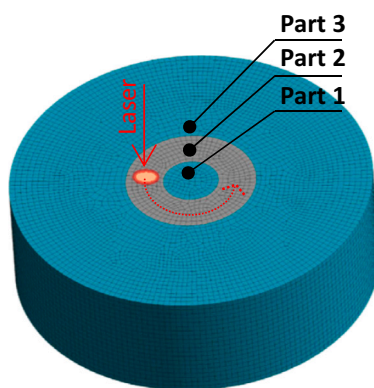


Fig. 8. The numerical model of the transient thermal simulation.

Table 2

The results of the first evaluation of the single-track weld's width. The marked samples are shown in the figure above.

TW (μm)		Laser Speed (mm/s)																				
		200	300	400	500	600	700	800	900	1000	1100	1200	1300	1400	1500	1600	1700	1800	1900	2000		
Laser Power (W)	175	353	310	261	290	246	221	214	199	223												
	200	401	343	303	286	317	271	240	210	201	210											
	225		374	309	271	255	214	203	199	174	163	145										
	250		344	314	270	253	233	223	201	180	161	163	159									
	275			380	346	332	289	262	277	235	227	221	201	149								
	300				305	325	308	267	260	232	223	202	211	193	183	192	186					
	325					333	316	275	274	262	258	207	199	200	196	189	176	168				
	350						358	336	328	317	300	261	259	259	205	200	199	209	205	352		
	375							317	308	201	372	370	272	267	250	287	230	237	239	223	217	
	400								357	332	358	301	273	234	236	223	214	206	223	216	212	201

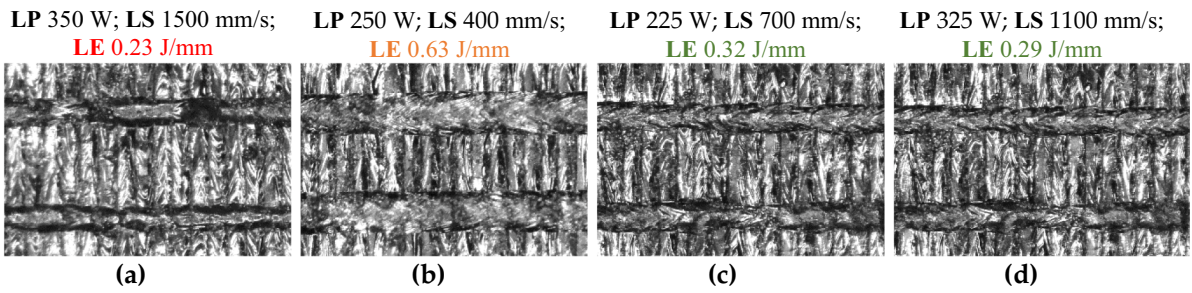
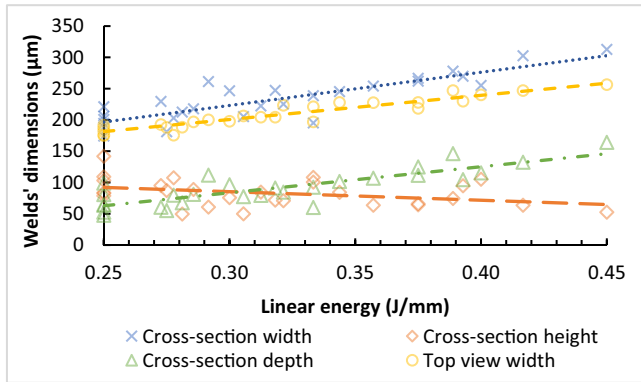
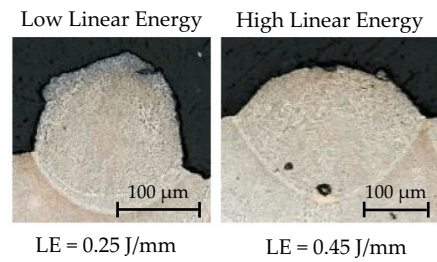


Fig. 9. The images of single-track welds captured by a digital-light microscope - (a) LE = 0.23 J/mm; (b) LE = 0.63 J/mm; (c) LE = 0.32 J/mm; (d) LE = 0.29 J/mm.

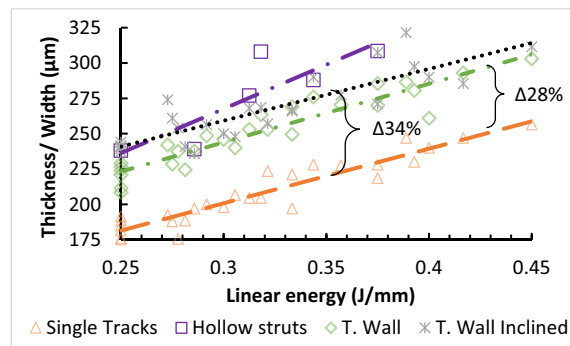


(a)

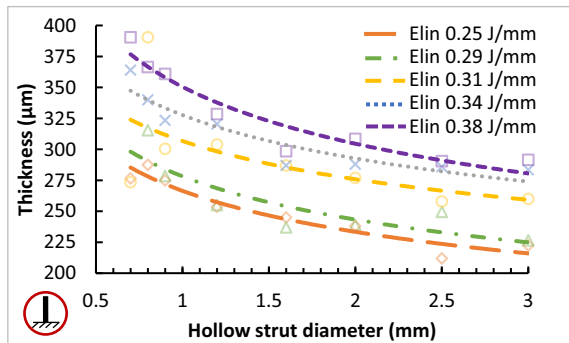


(b)

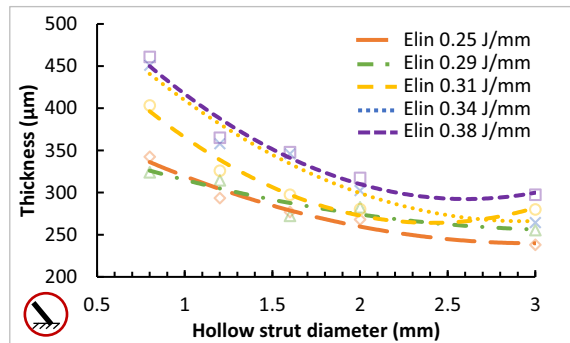
Fig. 10. (a) The geometrical parameters of the single-track welds vs. linear energy, (b) the examples of the typical shapes of the single-track welds.



(a)



(b)



(c)

Fig. 11. (a) The comparison of the single tracks width, hollow struts, and thin walls thickness, (b) the chart of the HT parameters vs. LE for vertical hollow struts (c) inclined hollow strut.

roughness. The numerical model represents the situation during the SLM production of the strut when a part of the strut was already produced, and the next layer is producing. The height of the model is 1 mm and consists of three parts for simulation of hollow strut experiment (Fig. 8). The Part 1 and Part 3 represent surroundings powder bed, and the Part 2 is solidified AlSi10Mg material. The mesh of all parts was created by the hex dominate Solid 90 elements with size of 0.05 mm (used layer thickness). Material parameters were used from Ansys Additive Manufacturing materials library and modified according to studies [25,32–34]. On the upper surface of all three parts the air convection was applied. The heat source (laser) was applied using the Moving Heat Source extension where the laser's circular trajectory was defined. The input energy was defined using LP and LS parameters. For simulation of full strut, the model was modified to consist only of Parts 2 and Parts 3. There is no powder in the centre part of the strut; therefore, Part 1 was removed, and Parts 2 was extended and filled the centre area of the strut.

3. Results

3.1. Laser process parameters window

Table 2 shows the results of the track width parameter (TW) measured by a digital-light microscope and the area of fine continuous track welds evaluated by a visual check (green area of the table). All samples were sorted according to the track weld's shape and quality into three types of colours. Fig. 9a shows the balling effect, which is typical for low input energy production (red colour). In Fig. 9b, the track weld's width is large and the height too low (orange colour). It was caused by the high input energy of the laser. In Fig. 9c,d, there is shown ideal situation when the single-track welds were continuous without any interruptions (green colour). The final perspective window is in the range of LP 200–350 W; LS 500–1400 mm/s; linear energy LE 0.25–0.4 J/mm.

The previous experiment was performed again for a deeper evaluation of the track welds' geometry using fine cross-sections images. The results are presented in Fig. 10a, where the strong dependence of the track welds' geometry on the LE is shown. The results show that due to the liquid melt pool's surface tension at a low energy level, the track weld's height is high, but the width and depth are low (Fig. 10b–low liner energy). With increasing LE, the track weld width and depth are growing, but the height is decreasing (Fig. 10b–high linear energy). The comparison of the track welds' width evaluated from the cross-sections and the digital-light microscope shows the same trend with deviation

caused by different evaluation approaches. In the cross-section case, the value of the width was measured accurately but only in one section of the track weld. It could cause small deviations compared to the average values measured by a digital-light microscope which are more representative for the whole track. Based on that, the microscope measurement's average values were further used. According to the study [21], the depth to width ratio was used to analyse the suitability of process parameters. This parameter was lower than 0.5 (–) for all tested process parameters, particularly in the range of 0.26–0.49. It means that those process parameters are suitable to produce components from AlSi10Mg material by SLM [16]. The obtained values will be used for comparison with modified experiments focused on lattice structure production.

3.2. Influence of samples geometry on track width

This experiment aimed to compare a walls thickness measured on the specific geometry of thin-wall and hollow strut with the single-track weld's width. The vertical walls' results were in the range of 209–303 μ m and showed a significant dependence on input linear energy (LE) as was the same in the case of single-track welds. The obtained values of the thickness were in average about 28% larger than TW values in the whole range of tested process parameters (Fig. 11a). In the case of inclined walls, the deviation was in average even 34% higher. The main reason is the lower heat transfer which decreases with the wall's inclination. Due to the low thermal conductivity of the surrounding powder bed, the energy is accumulated in the material and causes an increase in the wall thickness.

The results of the vertical hollow strut thickness (HT, diameter of 2 mm) had a similar trend as thin walls; however, the thickness was increasing at higher linear energies in comparison to thin walls. The cross-section images of inclined hollow struts showed the different thickness in the up-skin and down-skin areas (Fig. 12b). This deviation was probably caused by the thermal energy accumulation described above and in studies [12,16]. As is shown in Fig. 11c,d, the various nominal diameters of the hollow struts were produced using five levels of input linear energy (LE) in the range of 0.25–0.38 J/mm. The results showed that the HT parameter measured on a small diameter is larger compared to the HT parameter measured on a larger diameter, even if the same process parameters were used. The biggest differences were shown in the highest LE of 0.38 J/mm, where the HT parameter measured on the nominal diameter of 0.8 mm was 391 μ m and for the diameter of 3.0 mm was 292 μ m i.e., it is difference of 34%. In the case of

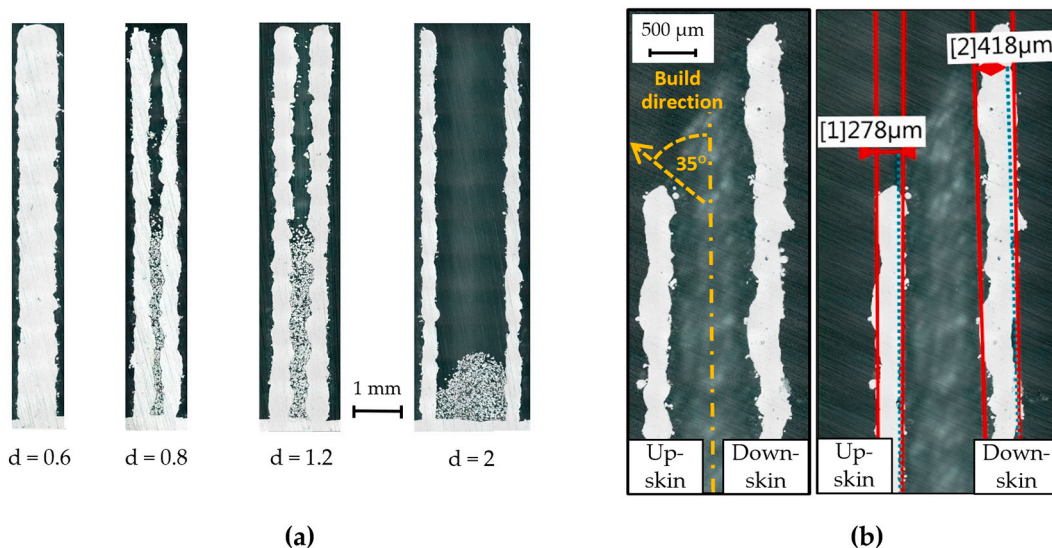


Fig. 12. (a) The digital-light microscope images of the vertical hollow strut cross-sections, (b) different up-skin and down-skin thickness measured on the metallographic cross-section of inclined hollow struts.

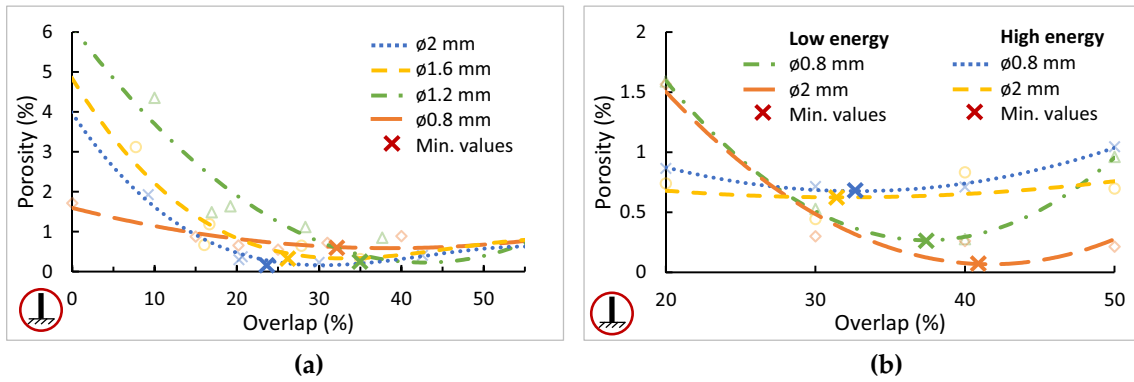


Fig. 13. The chart of porosity vs. overlap (a) OL in the range of 0–55%, (b) OL in range of 20–50%.

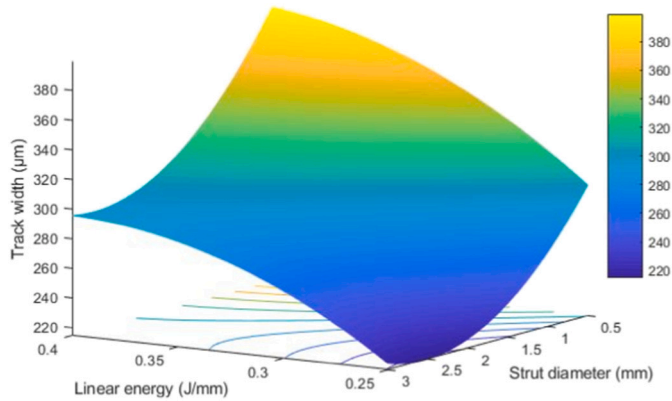


Fig. 14. Hollow strut's thickness vs. linear energy and strut diameter from Response surface analysis for vertical struts.

the diameters of 0.3–0.6 mm, both sides of the hollow strut were even connected, and a fully volumetric strut was created. These results are in line with the results presented by Dong et al. [11] where internal porosity and mechanical properties depend on the sample's diameter (up to 4 mm). The actual results clearly show that the deviation in the hollow strut's thickness and single tracks welds is significant. Therefore, it is necessary to implement HT parameter into the SLM laser strategy for lattice structure production to avoid internal defects.

3.3. Single-track weld overlap parameter

As it was mentioned above, the overlap (OL) parameter is expressed as percentage value of the hollow strut thickness (HT) and mainly affects the porosity in connection of two neighbouring tracks. Due to the small dimensions of lattice structures, the internal porosity influences their mechanical properties more than in case of bulk material; and therefore, the overlap is more important. The OL's correct setting is based on the HT parameter, which depends on dimensions of the lattice structure and the liner input energy (LE) of the SLM process.

The porosity values were measured in the transverse cross-section of hollow struts composed of two laser tracks. In Fig. 13a, the first loop of the experiment results is present. As it is shown, the porosity decreased

with increasing OL parameter, and the minimum value was reached in the range of 20–50% for all tested dimensions. The second loop was focused on the perspective range of 20–50%, and only limit values of previously tested parameters were used, i.e., diameters of 0.8, 2 mm (thin and large diameter representant) and LE of 0.25, 0.38 J/mm (low and high energy representant). The results showed that OL parameter is not dependent on the lattice structure's dimension but on LE (Fig. 13b). Therefore, the optimal OL values are in the range of 30–40% for all tested parameters (thin, large diameter; low, high energy).

3.4. Strut thickness prediction based on response surface analysis

As it is clear from previous results, the definition of the SLM process parameters for lattice structure manufacturing is complex task affected by input linear energy, size, and orientation of the lattice structure. To include the effects to the contour strategy parameters, the response surface analysis (RSA; part of the Design of Experiments) of the hollow strut thickness (HT) parameter was prepared. The RSA allowed determining the exact value of HT for specific input linear energy (LE) and the strut's nominal diameter (SD). The HT values were interpolated by the quadratic surface described by Eq. (3) with the reliability of R2 = 78% for vertical struts (Fig. 14) and by Eq. (4) with the reliability of R2 = 86% for inclined struts. Thus, it is possible to predict the values also for the parameters that were not tested exclusively.

The comparison of the RSA prediction and the measured data for the specific parameters are shown in Table 3 (vertical hollow struts, linear energy of 0.34 J/mm). The average deviation was 2.18%, and the largest deviation was 6.72% in the case of 0.9 mm strut diameter.

$$TH_{ver} = -134 + 2736 \cdot LE - 94.3 \cdot SD - 3177 \cdot LE^2 + 21.25 \cdot SD^2 - 54 \cdot LE \cdot SD \quad (\mu m) \tag{3}$$

$$TH_{inc} = -31 + 2450 \cdot LE - 101 \cdot SD - 2025 \cdot LE^2 + 35.8 \cdot SD^2 - 301 \cdot LE \cdot SD \quad (\mu m) \tag{4}$$

3.5. Full strut verification

In the following chapter, the previous results were used for the definition of the SLM contour strategy for lattice structure manufacturing and their influence was observed on the material porosity, surface roughness and the dimensional accuracy.

Table 3
The comparison of the response surface analysis data and measured values.

Strut Ø (mm)	0.7	0.8	0.9	1.2	1.6	2	2.5	3
Predicted HT (μm)	362.5	354.4	346.8	326.3	304.9	290.4	281.8	283.8
Measured HT (μm)	364	340	323.5	320.5	287	288	286	283.5
Deviation (%)	-0.4%	4.1%	6.7%	1.8%	5.9%	0.8%	-1.5%	0.1%

Table 4

The comparison of the vertical struts produced by the default SLM process parameters and the contour strategy (LP = 200 W, LS = 700 mm/s, LE = 0.29 J/mm).

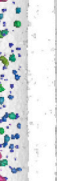
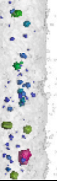
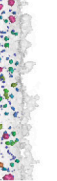
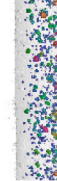
D_{nom} (mm)	0.6	0.7	0.8	0.9	1.0	1.25	1.5	2.0	3.0		
Por. (%)	1.74	1.79	1.97	1.92	1.9	0.97	0.78	0.24	0.06		
 Default											
	Por. (%)	0.02	0.23	0.36	0.64	0.69	0.32	0.05	0.04	0.09	
	CS 1 st loop										
		Por. (%)	0.01	0.01	0.09	0.07	0.02	0.01	0.01	0.01	0.04
		CS 2 nd loop									

Table 5

The comparison of the inclined struts produced by the default SLM process parameters and the contour strategy (LP = 200 W, LS = 700 mm/s, LE = 0.29 J/mm).

D_{nom} (mm)	0.6	0.7	0.8	0.9	1.0	1.25	1.5	2.0	3.0		
Por. (%)	0.11	0.13	1.11	1.44	1.16	2.04	1.64	0.88	0.25		
 Default											
	Por. (%)	0.24	0.25	0.54	0.38	0.09	0.62	0.58	0.64	0.47	
	CS 1 st test loop										
		Por. (%)	0.11	0.21	0.08	0.12	0.33	0.03	0.02	0.01	0.04
		CS 2 nd test loop									

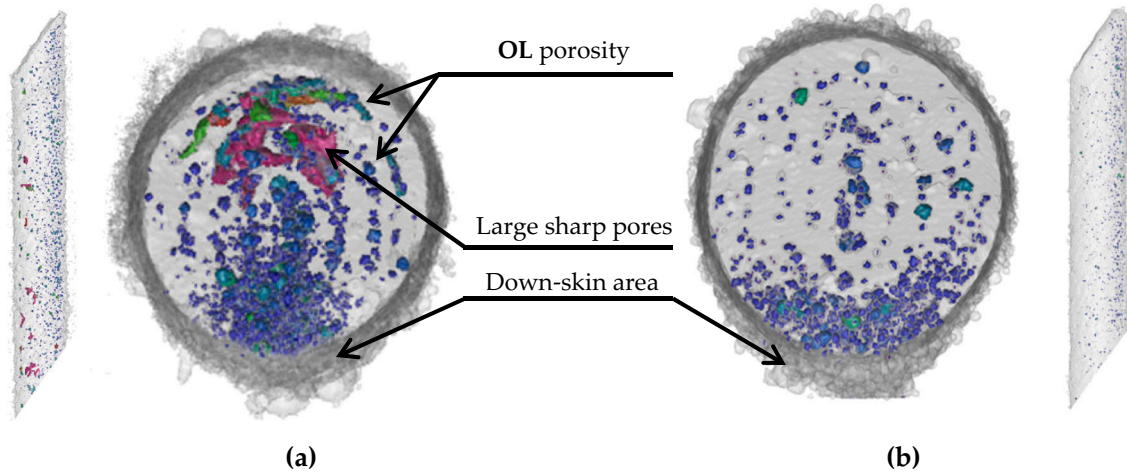


Fig. 15. (a) The top view of the inclined strut ($d = 2$ mm, $LP = 300$ W, $LS = 800$ mm/s, $LE = 0.38$ J/mm) (a) the first testing loop (b) the second testing loop.

3.5.1. Material porosity

The material porosity experiment was divided into two steps. In the first testing loop, the same parameters were used as in case of hollow struts experiment, i.e., the strut diameters and specific hollow strut thickness (HT) values (Fig. 11c). The reason was to minimise unexpected circumstances which could influence the results. The other contour strategy parameters were derived from the HT parameter, i.e., the distance of the contour trajectories $CD = HT - OL$, the contour overlap between the neighbouring track of 30% ($OL = 0.3 \times HT$), and the beam compensation $BC = 0.5 \times HT$. The material porosity measured by μ CT was chosen as the main response parameter.

The results of the first testing loop showed a relatively high level of porosity in thin vertical struts for all tested input linear energies (LE) (Fig. 16a,b). The default SLM process parameters with meander hatch strategy reached the porosity level of 2%; the contour strategy (CS) approach reached an interval between 0.16% and 1.35% based on the used LE. The porosity decreases according to LE and the strut nominal diameter. Tables 4 and 5 show the graphical comparison of the level and distribution of porosity obtained using meander hatch and the CS strategy. The meander hatch strategy led to a high porosity level with spherical and equally distributed pores in the whole volume. An exception was the large vertical struts ($d = 2$ and 3 mm), where the

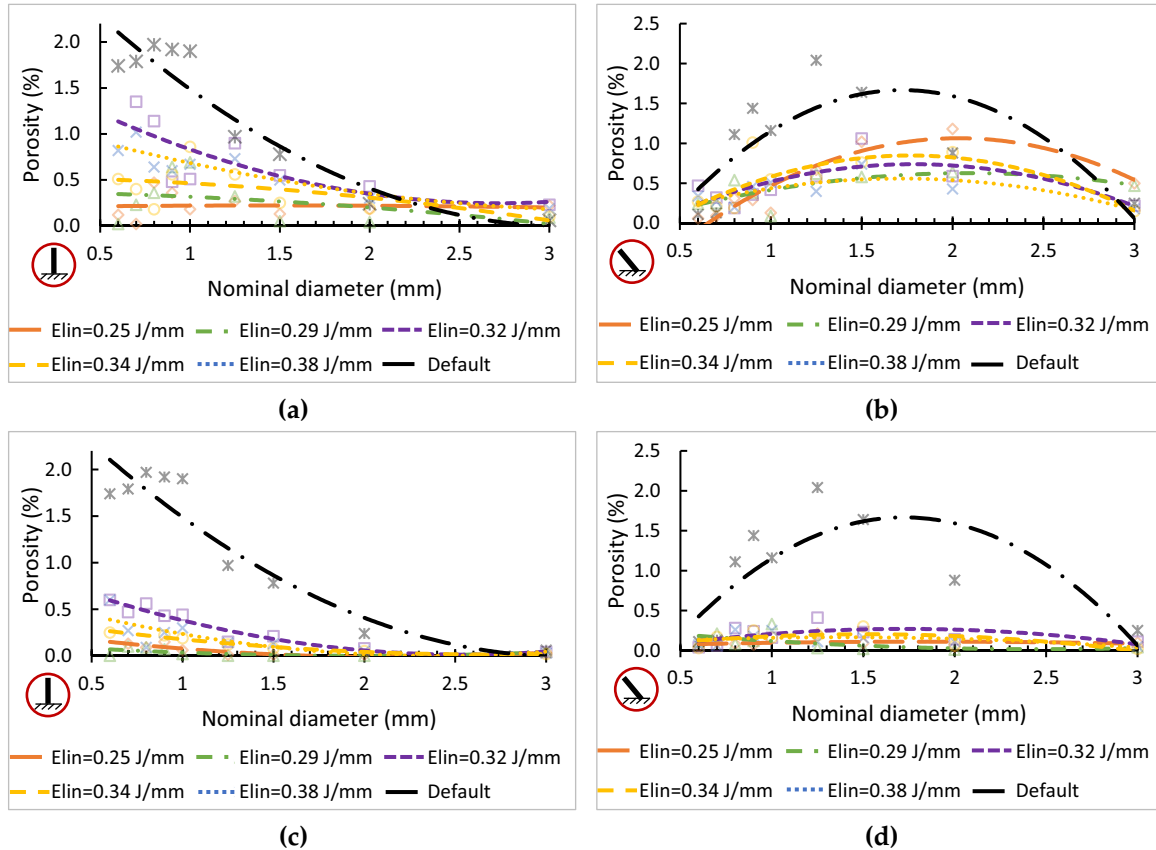


Fig. 16. Comparison of the meander and contour strategy (a) the level of porosity for the vertical struts (b) the level of porosity for the inclined struts in the first loop; (c), (d) second loop.

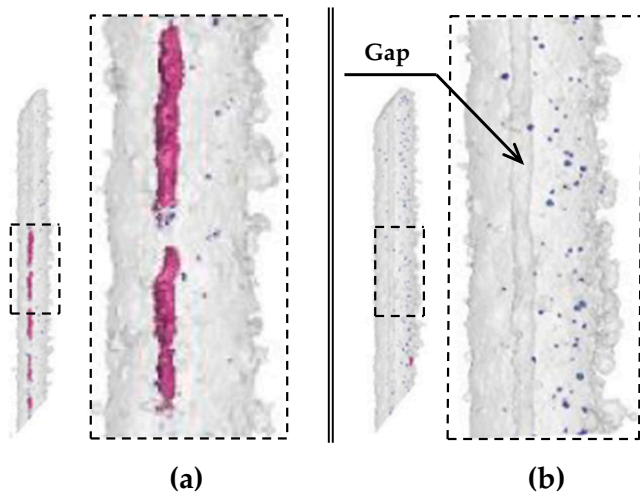


Fig. 17. The struts with non-melted pores in the middle axis area (a) LP = 225 W, LS = 900 mm/s, LE = 0.25 J/mm, OL of -10.65%; (b) LP = 300 W, LS = 800 mm/s, LE = 0.38 J/mm, OL of -11.28% (un-melted area in the strut axis).

porosity was low. It was caused by high thermal conductivity in larger struts that could be considered as bulk material for which the default process parameters are mostly optimised. A similar conclusion was reached by Dong et al. [11] for dimensions over 4 mm.

The CS porosity results were presented by the μ CT images of the struts produced with input linear energy LE = 0.29 J/mm (middle value from tested range). The CS approach showed a lower porosity level for both vertical and inclined thin struts (up to 1 mm). The porosity was equally distributed; however, its level grew with the increasing diameter of the strut, and large sharp pores occurred over the diameter of 1 mm. It relates to the direction of the contour track production and the number of tracks. The large struts (the diameter over 1 mm) consisted of 3 and more laser tracks (depends on used LE). It led to the lack of powder inside the strut if outside-in direction of the contour strategy was used. This was caused by drag of the surrounding powder into the melt pool during powder melting [35]. This effect relates to the change of the material state because the density of powder is much lower than melted material and therefore, larger volume of the powder is consumed for the melt pool. To minimise the effect, the inside-out direction will be used for the next test loops. Moreover, the sharp overlap porosity was found in the top view images (Fig. 15a). It could be created due to insufficient overlapping of neighbouring contour tracks in the up-skin area where the thickness of the track is thinner than in the down-skin area above the

powder bed. Based on that, the OL parameter was increased about 5% to 35% which stabilise the situation in up-skin area. But on the other hand, it can increase a porosity in the down-skin area.

The second testing loop showed significant improvement in all observed parameters. A change of laser scanning direction eliminated the sharp pores. The porosity level was significantly decreased using the hollow strut thickness (HT) obtained from Response Surface Analysis (RSA) and changing the OL to 35%. The results are shown in Figs. 16c, d and 15b, where the porosity level reached values in the interval of 0.01% (LE = 0.29 J/mm) to 0.6% (LE = 0.32 J/mm) for vertical struts and even in the interval of 0.07% (LE = 0.25 J/mm) to 0.4% (LE = 0.32 J/mm) for inclined struts. Tables 4 and 5 show the gradual evolution of the results and the clear positive effect of the CS strategy on all observed struts' parameters. The results also showed the issue with unmelted centre areas of some struts. If the non-compatible combination of the HT and strut diameter is used, the gap could occur in the strut centre (Table 5 - 1st loop d = 1.5 mm; 2nd loop d = 0.7 and 1.0 mm).

The last testing loop mainly aimed to reduce the unmelted area in the struts' centre (Fig. 17). Using RSA prediction, the optimal combination of the process parameter was found for each strut diameter. Thereby, the constant OL parameter was reached in the whole cross-section of the vertical and inclined struts (Table 6). The porosity results generally showed very low level of spherical porosity without unmelted areas, i.e., in case of inclined struts max. 0.16%; in case of vertical struts max. 0.19%. It confirms that the results of RSA analysis and OL parameter of 35% allow achieving very low values of porosity level for various diameters of the struts using different SLM parameters within the defined perspective process window.

Based on the results, the contour strategy and customisation of the process parameters for various dimensions of the lattice structure seem to be an effective approach to eliminate the material imperfections.

3.5.2. Dimensional accuracy

The results of the first testing loop are shown in Fig. 18a,b, where the dimensions of the struts are generally smaller than the nominal diameters. This issue could relate to the circular trajectory of the laser which means the higher laser speeds along the outer part of the trajectory due to its curvature (Fig. 20) and therefore HT parameter is thinner. It affects beam compensation parameter (BC; Fig. 1) which was too high and caused the dimensional deviations. Eq. (5) was created to reach the optimal dimensional accuracy based on the evaluation. Then, the BC parameter was changed to $BC = BC_{coef} \times TH$. The resulting $BC_{coef} = 0.34$ was further used in the next testing loops, which expressed the average value used for all strut diameters. BC_{coef} was evaluated based on the nominal strut diameter (SD) and diameter of the first peripheral

Table 6
The chosen results from the third validation testing loop.

	Vertical					Inclined				
	D _{nom} (mm)	0.6	0.8	1.25	2.0	3.0	0.6	0.8	1.25	2.0
LP (W)	214	325	243	263	263	171	251	263	263	263
LS (mm/s)	950	950	950	864	861	950	950	833	665	928
LE (J/mm)	0.23	0.34	0.26	0.30	0.31	0.18	0.26	0.32	0.40	0.28
Por. (%)	0.02	0.19	0.09	0.04	0.02	0.02	0.07	0.12	0.07	0.01
CS 3 th loop										

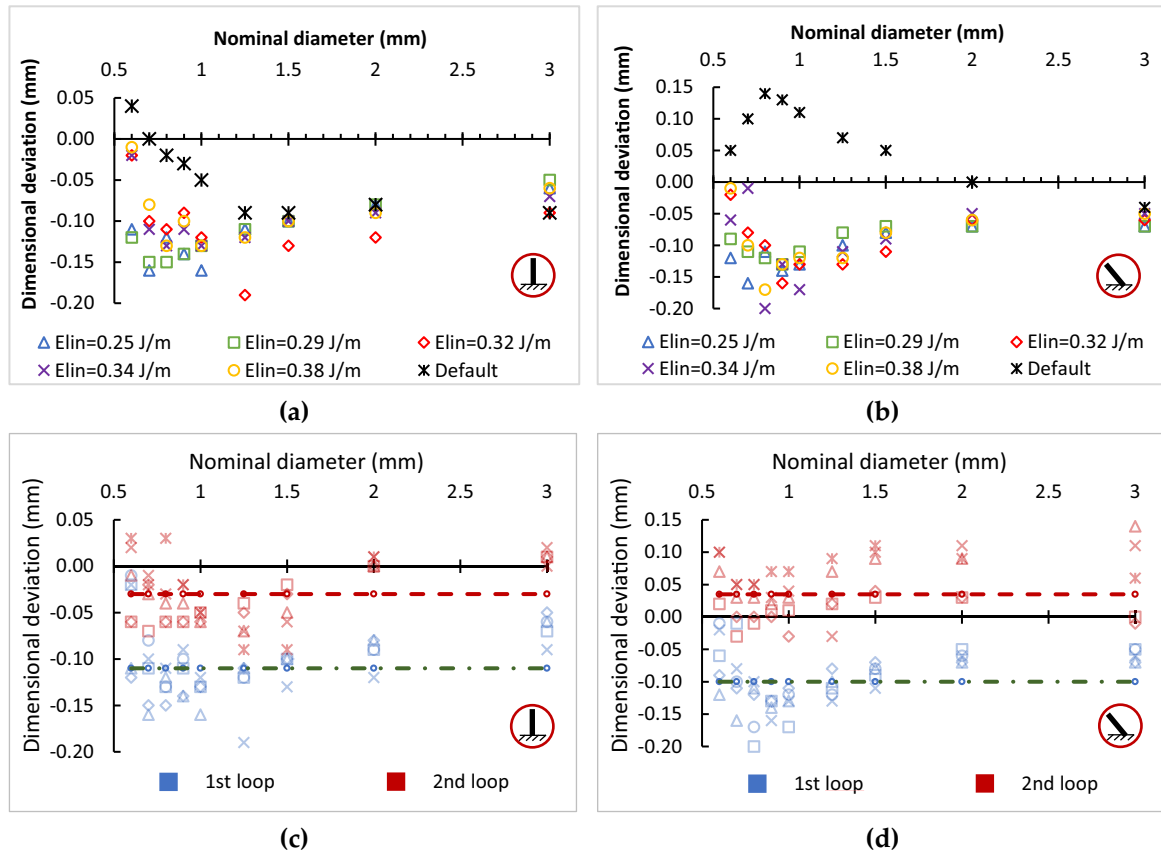


Fig. 18. The charts of the dimensional deviations from the nominal diameter of the first loop (a) vertical strut, (b) inclined strut; comparison between the first and second loop with marked median values for (c) vertical strut, (d) inclined strut.

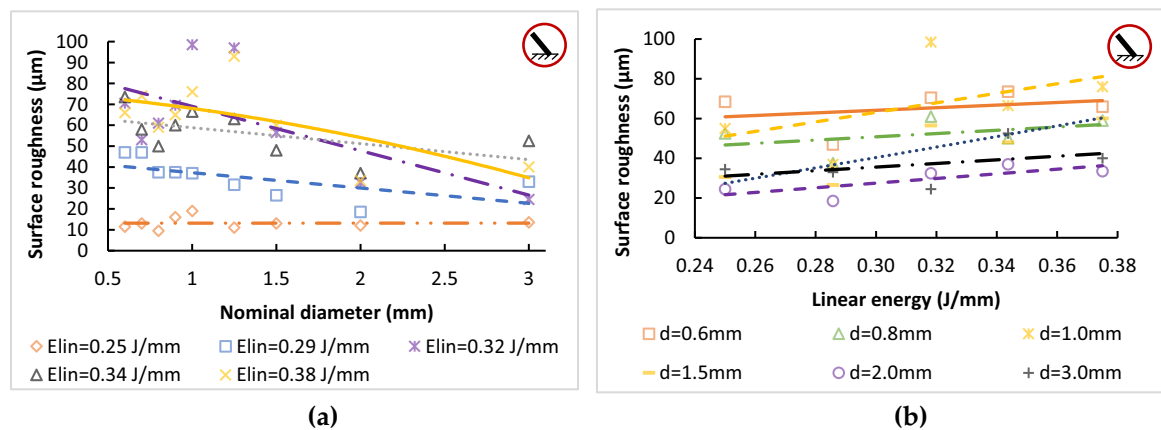


Fig. 19. The surface roughness (a) dependence on the dimensions of the strut (b) dependence on the linear energy.

contour track (PCD).

$$BC_{coef} = \left(\frac{SD - PCD}{2} \right) / HT \quad (-) \quad (5)$$

The modified BC parameter's influence is presented in Fig. 18c,d. As the comparative parameter between the first and second testing loop, the median value of the dimensional deviation was used. In the case of the vertical struts, the median value was changed from -0.11 mm to -0.03 mm. In the case of inclined struts, the median value changed from -0.10 mm to 0.04 mm. In both charts, two areas of results could be found. The dimensional deviations of the larger vertical struts are low. However, in the case of thin struts, the deviations are higher, and the

values are unstable. The inclination of the struts' leads to better accuracy in the case of thin struts, but on the other hand, the deviation of the larger struts is higher than in the first testing loop. In general, the change of the BC_{coef} parameter from 0.5 to 0.34 helped significantly reduce the dimensional deviations; however, to reach even better accuracy, the BC parameter must be evaluated individually according to the struts' size, the orientation of the struts and used LE.

3.5.3. Surface roughness

Surface roughness (R_a) was measured on the inclined struts' down skin surface where the R_a values are the highest [14]. The contour strategy approach shows the same trend for all levels of the tested LE, i.

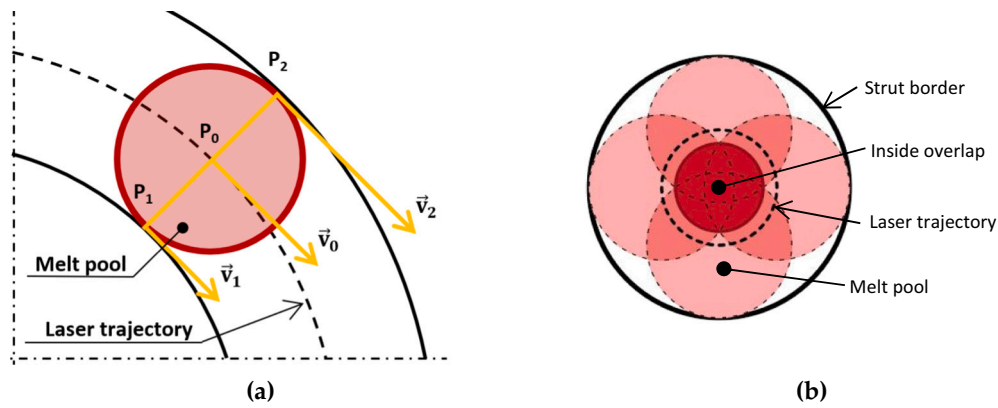


Fig. 20. (a) Schema of the circular trajectory influence on the change of the actual velocity of the melt pool, (b) Schema of the possible remelting in the thin struts [36].

e., the small diameters have relatively high Ra values, which decrease with the increasing size of the strut (Fig. 19). In higher linear energies, the differences between the small and large struts are more significant. This effect is related to the dissipation of thermal energy from the melt pool area and the size of the struts. With increasing LE, the surface roughness Ra increases linearly across all tested diameters (Fig. 19b). This conclusion matches with the study [16] where they focused on a wide range of LE and the strut diameter of 2 mm.

Surface roughness partially affects also dimensional deviations which can be seen by comparing the charts of Figs. 18 and 19a. The charts show that the struts with a small diameter have a larger deviation of the dimensions and higher surface roughness than larger struts.

4. Discussion

The presented results aimed to describe the SLM process's specific behaviour during the manufacturing of thin-strut lattice structure. Due to low volume of material, the lattice structures are highly affected by thermal behaviour of SLM melting process; therefore, the geometry and size of produced lattice structures must be considered. For this purpose, the Contour Strategy (CS) parameters was developed which led to elimination of typical imperfections of lattice structure, such as dimensional inaccuracy, high surface roughness and porosity.

4.1. The process of the contour strategy optimisation

4.1.1. Comparison of the single tracks, thin wall, and hollow struts results

The first differences have already appeared in the basic SLM

experiment, respectively, in comparison of the single-track welds and thin-walls, and hollow struts thickness results. The thin perpendicular walls' thickness was about 28% wider than the single-track welds' width, and the inclined walls was even 34% (Fig. 11a). The hollow strut's thickness showed a similar deviation as the inclined walls (Fig. 11b); however, more significant dependence on the input energy (LE) was observed. In previous studies [11,17], the need for similarity of the samples shape and final components was mentioned. Therefore, the hollow strut's geometry was finally used to design the CS parameters.

Based on the wider thickness of hollow strut samples, the hypothesis was created that the circular shape of the laser CS trajectory and their small diameter causes the changes in the melt pool's thermal behaviour. Due to a circular shape of laser trajectory with a very small diameter, the inner part of the melt pool moves slower than the outer part (Fig. 20). This locally increases the input energy Eqs. (8), (9) because the laser exposes the inner part of the strut longer and the melt pool expands. Then, the hollow strut's thickness increases faster than the walls with increasing input linear energy (LE; Fig. 11b). The example could be the set of the process parameters LP = 325 W, LS = 1100 mm/s Ein = 0.295 J/mm and the strut diameter d = 0.8 mm; due to the speed distortion on circular trajectory, the LE is distributed from Ein,1 = 0.535 J/mm to Ein,2 = 0.204 J/mm depend on the position.

$$v_1 = \frac{v_0 \cdot (d_0 - TH)}{d_0} = v_0 \cdot \frac{d_1}{d_0} \tag{6}$$

$$v_2 = \frac{v_0 \cdot (d + TH)}{d} = v_0 \cdot \frac{d_2}{d_0} \tag{7}$$

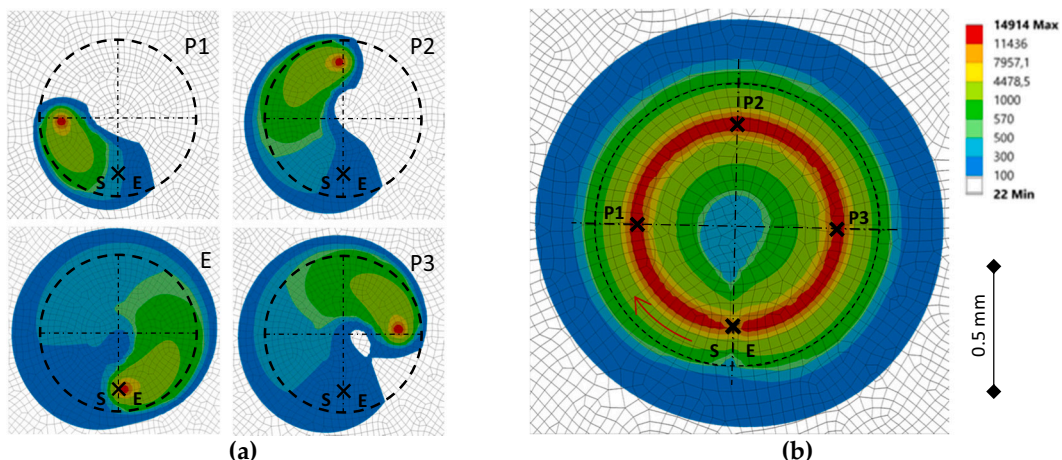


Fig. 21. (a) Laser heat affection of vertical strut geometry in four points of laser trajectory; (b) heat affection of whole strut.

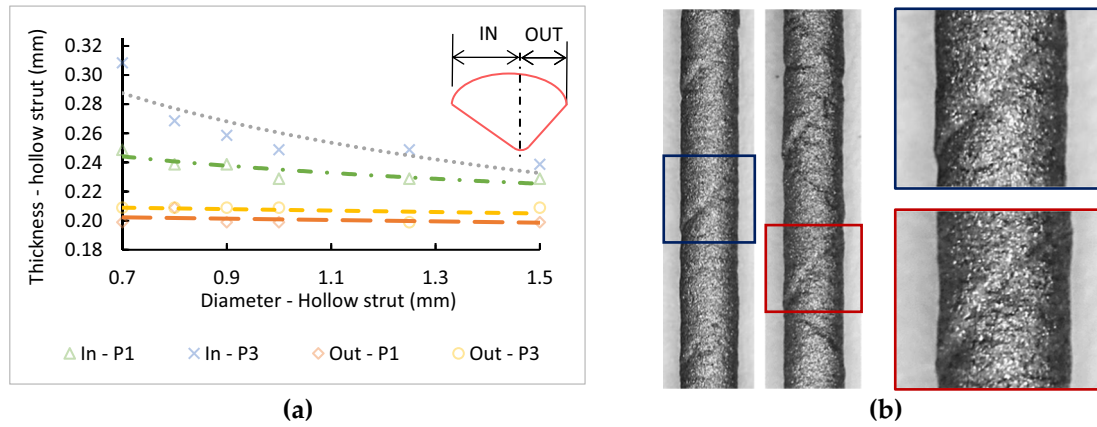


Fig. 22. (a) Strut thickness of the vertical struts with different strut diameter in three points of trajectory based on simulation; (b) spiral groove on surface of vertical struts.

$$E_{in,1} = \frac{P}{v_1} \tag{8}$$

$$E_{in,2} = \frac{P}{v_2} \tag{9}$$

The hypothesis was verified using the vertical struts' transient thermal simulation ($d = 0.8 \text{ mm}$) in Ansys Workbench software. The described phenomenon is associated with the strut diameter (Fig. 22a), input linear energy (Fig. 11c,d) and also the position on the laser trajectory (Fig. 21a,b). Close to the starting point (S), the laser started exposition and the melt pool is the narrowest. In the middle of the trajectory (point P2, P3), the track thickness (HT) is growing as the melt pool is larger and longer. In the last part of the trajectory, the melt pool meets the pre-heated area of the powder (around $300 \text{ }^\circ\text{C}$) and includes the biggest amount of melted material; the HT is the largest.

The magnifying of the melt pool is also visible on the strut surface where the spiral groove was formed (Fig. 22b). The groove is caused by the deviation of the HT parameter in the start/end point and the spiral shape was created due to moving of this point in each layer by 67° (default setup in post-processing software). Also, the asymmetry of the HT was observed especially in the centre of strut as was described above (Fig. 20).

Obtained results supported the hypothesis because the values of the LE and d dependence have the same trend as the numerical results. This phenomenon also affected the possibility of the small strut production. The smallest struts to produce are those with the diameter $d = 0.6 \text{ mm}$.

4.1.2. Overlap parameter and inter-weld porosity

The overlap (OL) is one of the key parameters that contribute for SLM manufacturing process stabilisation. The OL parameter defines the overlapping and connection of the neighbouring track welds. If the OL parameter is too high, the gas porosity occurs by vaporising the AlSi10Mg chemical components. Otherwise, if the OL parameter is too low, the lack of fusion porosity occurs because the gap between neighbouring track is filled by unmelted powder. Therefore, the inter-weld porosity was chosen as the main response parameter during OL optimisation and the aim was to minimise it.

The results showed that the minimum porosity value was achieved in the OL range of 30–40% of the hollow strut thickness (HT; Fig. 13b). According to the further results of the volumetric porosity, the optimal OL value of 35% was finally found. The reason was the lack of fusion porosity which was observed in the inclined strut. After modifying the OL parameter, this issue disappeared (Fig. 15a).

4.1.3. Design of the contour strategy parameters

The main design parameter for minimising the lattice structure imperfections is the hollow strut thickness (HT) that depending on the required strut's diameter, structure topology and the input linear energy (LE). The necessary condition is the constant overlap of 35% (OL) in the whole strut cross-section; therefore, the combination of the strut diameter and compatible HT parameter must be chosen to achieve the integer number of the laser contour even in the strut's centre. Otherwise, two typical issues appear. If the OL parameter is higher than 35%, the remelting of the material and gas porosity occurs in the strut centre. If the strut is unmelted in the centre (negative value of OL), the lack of fusion porosity occurs (Fig. 17b,c). Both issues significantly decrease the

Table 7
Different setup of contour strategy for inclined strut with a diameter of 1.25 mm; three sets of process parameters.

State	Optimal	Remelted	Unmelted
D_{nom} (mm)	1.25	1.25	1.25
LP (W)	350	275	300
LS (mm/s)	1100	800	800
LE (J/mm)	0.32	0.34	0.38
TH (μm)	354	272	392
OL in centre (%)	+36.5	+48.8	-11.3

The diagrams below the table illustrate the laser contour strategies for different OL values. The first diagram (+36.5%) shows a regular, overlapping contour pattern. The second diagram (+48.8%) shows a pattern where the contours overlap significantly, leading to remelting. The third diagram (-11.3%) shows a pattern where the contours do not overlap enough, leaving gaps (unmelted material) in the center.

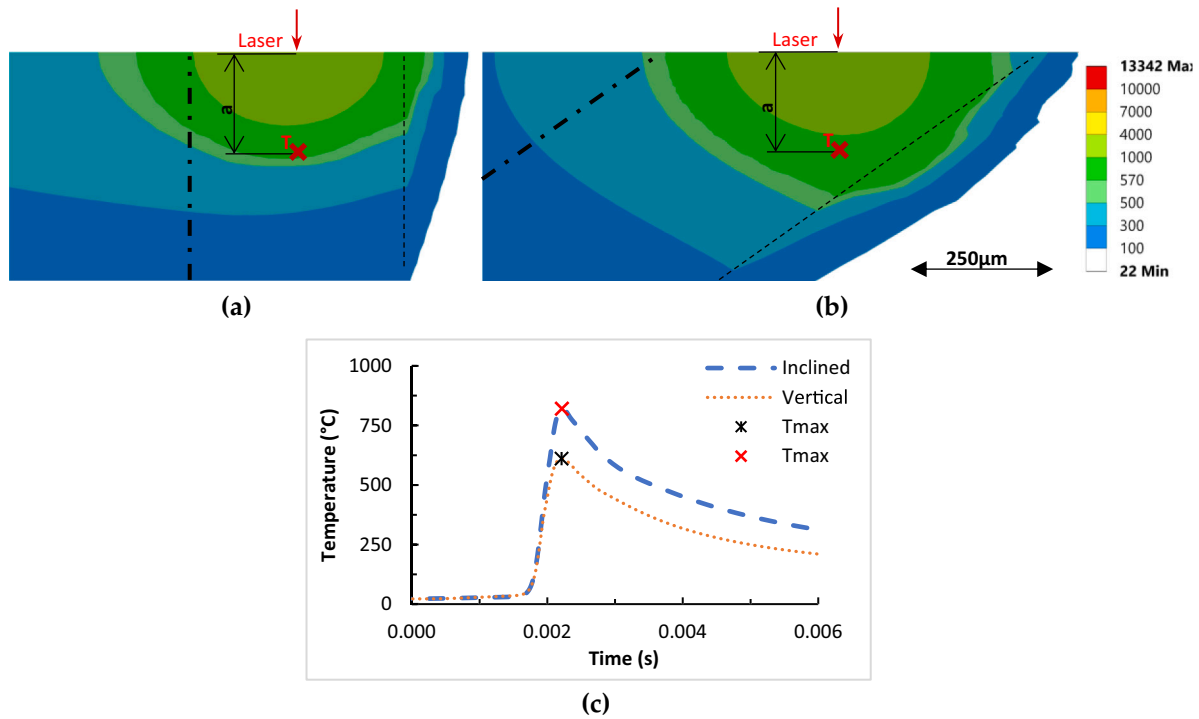


Fig. 23. The numerical simulation of the thermal distribution during powder melting (a) vertical strut; (b) inclined strut; (c) The chart of the temperature T in the distance a below laser exposing point in vertical and inclined strut (d = 0.4 mm).

mechanical properties of the lattice structures.

The results of the HT parameters were analysed using Response Surface Analysis (RSA). It allows finding a smooth approximation of the HT results in the whole perspective SLM process window, definition of their equations (Eqs. (3), (4)), and finally describe the dependence of LE-d-TH parameters for both perpendicular and inclined struts. These predictions make it possible to effectively find the optimal parameters depending on the produced strut diameter (0.6 - 3 mm), input energy (LE 0.25–0.38 J/mm) and orientation. Using the specific values of the HT parameter for each combination of the SLM process parameters and strut diameter enables to obtain the best possible quality of produced lattice structures and implement all previous results into the CS (Table 7).

4.2. The higher level of porosity and surface roughness in inclined struts

The SLM process is based on the selective melting of the metal powder by a high-power laser. The layer-by-layer production causes a cyclic thermal loading of the manufactured part that must be dissipated from the melting point through the component. The crucial moment of

the SLM process is the melting of the powder. During the solidification of a liquid phase, the material microstructure is created. If the temperature is too high or low in the melt pool, the internal porosity is formed. However, the situation is different in the inclined and vertical struts due to their orientation.

During the vertical struts production, the laser points in the direction of the strut's axis, and there is the volumetric material below the melt pool. Surrounding powder material is not significantly influenced by thermal energy (Fig. 23a). Another situation is in the case of the inclined strut. The laser does not point in the direction of the axis but in the Z-direction. This causes the root of the melt pool also points in the Z-direction and thermally influence the down-skin area of the strut where high surface roughness is formed (Fig. 23b). The surrounding powder has low thermal conductivity therefore, it prevents heat dissipation to the surroundings. Thermal energy is longer trapped in the melt pool and then dissipated to the volumetric material with higher thermal conductivity. It follows that the down-skin area of the strut is more thermally influenced than the up-skin area of the strut. Moreover, due to layer-by-layer production, this situation is repeated many times and the changes of microstructures, and material porosity occur [12].



Fig. 24. Microstructure of the struts [16] (a) LP 250 W, LS 1400 mm/s, Ein 0.18 J/mm; (b) LP 300 W, LS 500 mm/s, Ein 0.6 J/mm.

The porosity results in Fig. 15 confirmed this hypothesis. In Fig. 15a, there are many small gas pores placed in the down-skin area even the lack of fusion porosity has appeared in the up-skin area. As was explained above, the down-skin area is repeatedly remelted; therefore, the negative effect of low input energy disappeared and is observable only in the up-skin area. A similar situation is presented in metallographic cross-sections of the previous study [16]. Even the strut was produced by the process parameter out of the recommended process window, the metallographic pores are placed in the down-skin area especially when the high input energy is used (Fig. 24b). In the up-skin area, the lack of fusion porosity appears as was expected (Fig. 24a).

4.3. Influence of contour strategy on mechanical properties

As described above, the contour laser strategy has a positive effect on reducing porosity, surface roughness, and dimensional accuracy. These imperfections mainly cause the initialization of cracks during the mechanical loading of produced parts. Especially, porosity situated near the surface is very susceptible to the initialization of crack. In the case of lattice structure with struts diameter of 0.5–3 mm, the porosity highly affects the strut's cross-section and has a high impact on mechanical properties [9,12,27]. Surface roughness has a similar effect as subsurface porosity. A highly rough surface can cause crack initiation, especially in the bottom area of the inclined strut [14,15]. Dimensional accuracy can affect the mechanical properties of lattice structures because produced struts do not reach the designed dimension (Fig. 18). The designed part could have a different mechanical property than were expected.

However, the microstructure can also be affected by scanning strategy and process parameters [37,38]. The scanning strategy can affect the mechanical properties of produced parts due to grain structure and orientation. Simultaneously, the energy of input parameters has an impact on microstructure. The contour strategy allows the setup of process parameters with different input energy. The contour strategy effect on lattice structures material microstructure and mechanical properties should be further explored.

5. Conclusions

The complex study about manufacturing of the SLM lattice structures was conducted to investigate the influence of the contour laser strategy (CS) on the material porosity, surface roughness, and dimensional accuracy of the lattice structures. Based on the investigation, the following conclusions can be listed below:

- The strong dependence of single-track welds parameters was observed on the specific geometry of the samples; therefore, it is necessary to use the results of the hollow struts thickness (HT) to design the CS parameters.
- The hollow struts thickness (HT) is a variable parameter that depends on the lattice structure's geometry, i.e., orientation and diameter of the struts, and the input linear energy (LE). The equations (Eqs. (3), (4)) were found that consider the relationship between the parameters.
- The overlap parameter of OL = 35% was evaluated for AlSi10Mg material as optimal to achieve the material porosity's best results for two struts orientations (vertical; inclined 35.26°). The constant OL must be reached in the whole volume of the struts, especially in the centre of the struts.
- The inside-out contour strategy significantly reduced the sharp pores caused by the lack of powder effect in the struts' centre.
- Using the found equations (Eqs. (3), (4)) of the hollow struts thickness dependence allows to find the optimal SLM process parameters for the required strut diameter and to minimise the material porosity under the level of 0.2% in the range of $d = 0.6\text{--}3.0$ mm.

- The inclined struts' surface roughness has a linear dependence on the input linear energy, and the values increased with higher energy. The contour strategy approach allows decreasing the surface roughness compared to default parameters. The maximum obtained values were Ra up to 16 μm for vertical struts and up to 80 μm for inclined struts.
- The contour strategy improves the diameter accuracy and the median value of dimensional deviations of 0.03 mm was reached for inclined struts and 0.04 mm for vertical struts.

Declaration of competing interest

The authors declare that they have no known competing financial interests or personal relationships that could have appeared to influence the work reported in this paper.

Acknowledgement

This work is a result of the research project *Architected materials designed for additive manufacturing (ArMAdit)* CZ.02.1.01/0.0/0.0/16.025/0007304, specific research project *FSI-S-20-6296*, the project *CEITEC 2020 (LQ1601)* with financial support from the Ministry of Education, Youth and Sports of the Czech Republic under the *National Sustainability Programme II* and *CzechNanoLab Research Infrastructure* supported by MEYS CR (LM2018110).

References

- [1] Vrána R, Koutný D, Paloušek D, Zikmund T. Impact resistance of lattice structure made by selective laser melting from AlSi12 alloy. *MM Science Journal* 2015; 852–5. https://doi.org/10.17973/MMSJ.2015_12_201547.
- [2] Meng G, Ji B, Han H, Gu C, Lin R, Peng F. Design and simulation of an innovative cylinder fabricated by selective laser melting. *Chinese Journal of Aeronautics* 2019; 32(1):133–42. <https://doi.org/10.1016/j.cja.2018.10.011>.
- [3] Stolt R, Elgh F. Introducing design for selective laser melting in aerospace industry. *Journal of Computational Design and Engineering* 2020;7(4):489–97. <https://doi.org/10.1093/jcde/qwaa042>.
- [4] Strecker Z, Kubik M, Vitek P, Roupec J, Paloušek D, Šreibr V. Structured magnetic circuit for magnetorheological damper made by selective laser melting technology. *Smart Materials and Structures* 2019;28. <https://doi.org/10.1088/1361-665X/ab0b8e>.
- [5] Maamoun AH, Xue YF, Elbestawi MA, Veldhuis SC. Effect of selective laser melting process parameters on the quality of Al alloy parts: powder characterization, density, surface roughness, and dimensional accuracy. *Materials* 2018;11. <https://doi.org/10.3390/ma1122343>.
- [6] Galy C, Le Guen E, Lacoste E, Arvieu C. Main defects observed in aluminum alloy parts produced by SLM: from causes to consequences. *Additive Manufacturing* 2018;22:165–75. <https://doi.org/10.1016/j.addma.2018.05.005>.
- [7] Pauly S, Schrickler C, Scudino S, Deng L, Kühn U. Processing a glass-forming Zr-based alloy by selective laser melting. *Materials and Design* 2017;135:133–41. <https://doi.org/10.1016/j.matdes.2017.08.070>.
- [8] Thijs L, Kempen K, Kruth JP, Van Humbeeck J. Fine-structured aluminium products with controllable texture by selective laser melting of pre-alloyed AlSi10Mg powder. *Acta Materialia* 2013;61:1809–19. <https://doi.org/10.1016/j.actamat.2012.11.052>.
- [9] Kempen K, Thijs L, Van Humbeeck J, Kruth JP. Mechanical properties of AlSi10Mg produced by selective laser melting. *Physics Procedia* 2012;39:439–46. <https://doi.org/10.1016/j.phpro.2012.10.059>.
- [10] Aboulkhair NT, Everitt NM, Ashcroft I, Tuck C. Reducing porosity in AlSi10Mg parts processed by selective laser melting. *Additive Manufacturing* 2014;1:77–86. <https://doi.org/10.1016/j.addma.2014.08.001>.
- [11] Dong Z, Zhang X, Shi W, Zhou H, Lei H, Liang J. Study of size effect on microstructure and mechanical properties of AlSi10Mg samples made by selective laser melting. *Materials* 2018;11. <https://doi.org/10.3390/ma1122463>.
- [12] Delroisse P, Jacques PJ, Maire E, Rigo O, Simar A. Effect of strut orientation on the microstructure heterogeneities in AlSi10Mg lattices processed by selective laser melting. *Scripta Materialia* 2017;141:32–5. <https://doi.org/10.1016/j.scriptamat.2017.07.020>.
- [13] Liu M, Takata N, Suzuki A, Kobashi M. Microstructural characterization of cellular AlSi10Mg alloy fabricated by selective laser melting. *Materials & Design* 2018;157: 478–91. <https://doi.org/10.1016/j.matdes.2018.08.005>.
- [14] Han X, Zhu H, Nie X, Wang G, Zeng X. Investigation on selective laser melting AlSi10Mg cellular lattice strut: molten pool morphology, surface roughness and dimensional accuracy. *Materials* 2018;11. <https://doi.org/10.3390/ma11030392>.
- [15] Tian Y, Tomus D, Rometsch P, Wu X. Influences of processing parameters on surface roughness of hastelloy X produced by selective laser melting. *Additive Manufacturing* 2017;13:103–12. <https://doi.org/10.1016/j.addma.2016.10.010>.

- [16] Vrána R, Koutný D, Paloušek D, Pantělejev L, Jaroš J, Zikmund T, et al. Selective laser melting strategy for fabrication of thin struts usable in lattice structures. *Materials* 2018;11. <https://doi.org/10.3390/ma11091763>.
- [17] Vrána R, Cervinek O, Mañas P, Koutny D, Paloušek D. Dynamic loading of lattice structure made by selective laser melting-numerical model with substitution of geometrical imperfections. *Materials* 2018;11. <https://doi.org/10.3390/ma11112129>.
- [18] Vrána R, Koutný D, Paloušek D, Zikmund T. Influence of selective laser melting process parameters on impact resistance of lattice structure made from AISI10Mg. In: Vol. 1. European Congress and Exhibition on Powder Metallurgy. European PM Conference Proceedings; 2016. p. 6.
- [19] Vrana R, Vaverka O, Koutny D, Docekalova K, Palousek D. Shape and dimensional analysis of lattice structures produced by selective laser melting. *MM Science Journal* 2020;2020:3938–42. https://doi.org/10.17973/MMSJ.2020_06_2020013.
- [20] Großmann A, Gosmann J, Mittelstedt C. Lightweight lattice structures in selective laser melting: design, fabrication and mechanical properties. *Materials Science and Engineering: A* 2019;766:138356. <https://doi.org/10.1016/j.msea.2019.138356>.
- [21] Aboulkhair NT, Maskery I, Tuck C, Ashcroft I, Everitt NM. On the formation of AISI10Mg single tracks and layers in selective laser melting: microstructure and nano-mechanical properties. *Journal of Materials Processing Technology* 2016; 230:88–98. <https://doi.org/10.1016/j.jmatprotec.2015.11.016>.
- [22] Yu G, Gu D, Dai D, Xia M, Ma C, Shi Q. On the role of processing parameters in thermal behavior, surface morphology and accuracy during laser 3D printing of aluminum alloy. *Journal Of Physics D-Applied Physics* 2016;49:135501. <https://doi.org/10.1088/0022-3727/49/13/135501>.
- [23] Zhang J, Song B, Wei Q, Bourell D, Shi Y. A review of selective laser melting of aluminum alloys: Processing, microstructure, property and developing trends. *Journal of Materials Science & Technology* 2019;35(2):270–84. <https://doi.org/10.1016/j.jmst.2018.09.004>.
- [24] Kempen K, Thijs L, Van Humbeeck J, Kruth J-P. Processing AISi10Mg by selective laser melting: parameter optimisation and material characterisation. *Materials Science and Technology* 2015;31(8):917–23. <https://doi.org/10.1179/1743284714Y.0000000702>.
- [25] Pei W, Zhengying W, Zhen C, Junfeng L, Shuzhe Z, Jun D. Numerical simulation and parametric analysis of selective laser melting process of AISI10Mg powder. *Applied Physics A* 2017;123:1–15. <https://doi.org/10.1007/s00339-017-1143-7>.
- [26] Louvis E, Fox P, Sutcliffe CJ. Selective laser melting of aluminium components. *Journal of Materials Processing Technology* 2011;211(2):275–84. <https://doi.org/10.1016/j.jmatprotec.2010.09.019>.
- [27] Qiu C, Yue S, Adkins NJE, Ward M, Hassanin H, Lee PD, et al. Influence of processing conditions on strut structure and compressive properties of cellular lattice structures fabricated by selective laser melting. *Materials Science and Engineering: A* 2015;628:188–97. <https://doi.org/10.1016/j.msea.2015.01.031>.
- [28] Großmann A, Mölleney J, Frölich T, Merschroth H, Felger J, Weigold M, et al. Dimensionless process development for lattice structure design in laser powder bed fusion. *Materials & Design* 2020;194:1–16. <https://doi.org/10.1016/j.matdes.2020.108952>.
- [29] Lei H, Li C, Meng J, Zhou H, Liu Y, Zhang X, et al. Evaluation of compressive properties of SLM-fabricated multi-layer lattice structures by experimental test and μ -CT-based finite element analysis. *Materials & Design* 2019;169:107685. <https://doi.org/10.1016/j.matdes.2019.107685>.
- [30] Li C, Lei H, Zhang Z, Zhang X, Zhou H, Wang P, et al. Architecture design of periodic truss-lattice cells for additive manufacturing. *Additive Manufacturing* 2020;34:101172. <https://doi.org/10.1016/j.addma.2020.101172>.
- [31] Zikmund T, Šalplachta J, Zatočilová A, Břínek A, Pantělejev L, Štěpánek R, et al. Computed tomography based procedure for reproducible porosity measurement of additive manufactured samples. *NDT & E INTERNATIONAL* 2019;103:111–8. <https://doi.org/10.1016/j.ndteint.2019.02.008>.
- [32] Letenneur M, Kreitchberg A, Brailovski V. Optimization of laser powder bed fusion processing using a combination of melt pool modeling and design of experiment approaches: density control. *Journal of Manufacturing and Materials Processing* 2019;3. <https://doi.org/10.3390/jmmp3010021>.
- [33] Liu S, Zhu H, Peng G, Yin J, Zeng X. Microstructure prediction of selective laser melting AISI10Mg using finite element analysis. *Materials & Design* 2018;142: 319–28. <https://doi.org/10.1016/j.matdes.2018.01.022>.
- [34] Du Y, You X, Qiao F, Guo L, Liu Z. A model for predicting the temperature field during selective laser melting. *Results in Physics* 2019;12:52–60. <https://doi.org/10.1016/j.rinp.2018.11.031>.
- [35] Metel A, Stebulyanin M, Fedorov S, Okunkova A. Power density distribution for laser additive manufacturing (SLM): potential, fundamentals and advanced applications. *Technologies* 2019;7. <https://doi.org/10.3390/technologies7010005>.
- [36] Großmann A, Felger J, Frölich T, Gosmann J, Mittelstedt C. Melt pool controlled laser powder bed fusion for customised low-density lattice structures. *Materials & Design* 2019;181:108054. <https://doi.org/10.1016/j.matdes.2019.108054>.
- [37] Liu X, Zhao C, Zhou X, Shen Z, Liu W. Microstructure of selective laser melted AISI10Mg alloy. *Materials & Design* 2019;168:107677. <https://doi.org/10.1016/j.matdes.2019.107677>.
- [38] Wang YC, Lei LM, Shi L, Wan HY, Liang F, Zhang GP. Scanning strategy dependent tensile properties of selective laser melted GH4169. *Materials Science and Engineering A* 2020;788:139616. <https://doi.org/10.1016/j.msea.2020.139616>.